Phase Synchronization of the El Niño-Southern Oscillation with the Annual Cycle

Karl Stein, Axel Timmermann, and Niklas Schneider

Phys. Rev. Lett. **107**, 128501 — Published 13 September 2011

DOI: 10.1103/PhysRevLett.107.128501

Phase synchronization of the El Niño-Southern Oscillation with the annual cycle

Karl Stein

Department of Oceanography, School of Ocean and Earth Science and Technology, University of Hawaii at Manoa

Axel Timmermann and Niklas Schneider

International Pacific Research Center & Department of Oceanography, School of Ocean and Earth Science and Technology, University of Hawaii at Manoa

(Dated: June 21, 2011)

Abstract

The El Niño-Southern Oscillation (ENSO) is the largest global climate signal on the interannual timescale. ENSO events occur irregularly, yet individual events follows a similar pattern of developing during boreal summer/fall and peaking during boreal winter. This characteristic of ENSO is often referred to as "phase locking" of ENSO with the annual cycle. However, no observational evidence of phase interaction between the two phenomena has thus far been presented. In this study, we analyze sea surface temperature observations and find the first evidence of partial phase synchronization of ENSO with the annual cycle.

The El Niño-Southern Oscillation (ENSO), which arises from coupled feedbacks within the equatorial Pacific ocean-atmosphere system, is the largest global climate signal on interannual timescales [1]. ENSO is characterized by large-scale changes in equatorial Pacific sea surface temperature (SST), atmospheric circulation, and precipitation. During El Niño events, the eastern Pacific SST is anomalously warm, the easterly trade winds along the equator weaken or even reverse, and areas of convective precipitation move eastward and equatorward. Cool La Niña events are marked by roughly opposite anomalies, though asymmetries exist between the two phases. The change in the tropical Pacific climate during strong ENSO events is large enough to influence the global atmospheric circulation, leading to significant environmental and socioeconomic impacts that occur in areas throughout the world [2]. ENSO events occur irregularly, with 2-7 year spans between them, but they each follow a similar pattern of developing during boreal summer/fall and peaking during boreal winter [3]. This feature has often been referred to as "phase locking" of ENSO to the annual cycle (e.g., [4–8]); however, observational evidence of phase interaction between the two phenomena has yet to be presented.

Current theory regarding the seasonal synchronization of ENSO events distinguishes between two paradigms: *frequency/phase* modulation or *amplitude* modulation. The former paradigm is based on the assumption that ENSO can be best described as a nonlinear deterministic system [9, 10] and the seasonal synchronization of ENSO events is seen as the result of frequency locking of ENSO to given periodic forcing by the seasonal cycle [11–13]. The second paradigm is based on the notion that ENSO can be described as a linear oscillation and its seasonal amplitude modulation results from the annual variation of the background state [14–16]. Thus, determining the relative importance of these two processes in the natural system would provide an important means to evaluate and improve ENSO theory and prediction models. The following analysis presents the first evidence from observations of partial 2:1 phase synchronization of ENSO to the annual cycle.

The data set analysed here is the UK Met Office Hadley Centre's 1° gridded SST analyses (HadISST [17]), with a spatial domain of 20°S-20°N, 120-290°E, and a temporal domain of 1964 - 2007. We denote the spatio-temporal data set as $\mathbf{s}(t)$, where the vector components represent the individual spatial grid points and t is time. To extract the tropical Pacific annual cycle and ENSO signals from this data set, we perform complex empirical orthogonal function (CEOF) analysis [18], which aims to capture the majority of the variability within

$\mathbf{s}(t)$ as the summation of a small number of empirically derived modes.

To begin, we calculate the analytical signal $\mathbf{b}$ of the spatio-temporal data set $\mathbf{s}(t)$. In vector notation, we obtain

$$\mathbf{b}(t) = \mathbf{s}(t) + i\,\mathcal{H}[\mathbf{s}(t)],$$

where $\mathcal{H}[...]$ is the Hilbert transform, $i = \sqrt{-1}$, and the vector time series $\mathbf{s}(t)$ has been zero-centered and any linear trends have been removed from each spatial component. The spatial covariance matrix of the analytical signal vector $\mathbf{b}(t)$ is then given by

$$\mathbf{C} = \langle \mathbf{b}^*(t) \otimes \mathbf{b}(t) \rangle_t,$$

where $\langle ... \rangle_t$ denotes time averaging and the asterisk denotes complex conjugation. Because $\mathbf{C}$ is self-adjoint, it possess real eigenvalues λ_n and complex eigenvectors $\mathbf{e}_n = (e_{n,j})$ with $j = 1, ...N$, representing the N spatial data points. The complex eigenvectors of $\mathbf{C}$ correspond to the spatial fields in the EOF representation of $\mathbf{b}(t)$, which is written as

$$\mathbf{b}(t) = \sum_n \alpha_n(t)\ \mathbf{e}_n^*,$$

where the complex principal component time series $\alpha_n(t)$ are computed via the projection $\alpha_n(t) = \sum_x \mathbf{b}(t) \cdot \mathbf{e}_n$. The vectors can be normalized such that

$$\langle \alpha_n \alpha_m^* \rangle_t = \delta_{nm}$$

$$\mathbf{e}_n \cdot \mathbf{e}_m^* = \lambda_n \delta_{nm},$$

where δ_{nm} is Kronecker's delta. As a shorthand, we will refer to the combination of the principal component time series $\alpha_n(t)$ and the spatial vectors $\mathbf{e}_n$ as the n-th mode of the CEOF representation. The fraction of the total data set variance associated with the n-th mode is given by $\lambda_n / \sum \lambda_m$ [19]. By convention, the first mode accounts for the largest amount of variance in $\mathbf{b}(t)$, the second mode the second largest amount of variance, and so on.

Because both the eigenvectors as well as the principal components are complex, one can obtain a magnitude and phase for both the spatial fields and time series of each mode via a Cartesian to polar coordinate transformation. For each spatial component j of the vector field we obtain:

$$q_{n,j} = \sqrt{Re[e_{n,j}]^2 + Im[e_{n,j}]^2}, \quad r_{n,j} = \arctan \frac{Im[e_{n,j}]}{Re[e_{n,j}]}$$

$$\sigma_n(t) = \sqrt{Re[\alpha_n]^2 + Im[\alpha_n]^2}, \quad \phi_n(t) = \arctan \frac{Im[\alpha_n]}{Re[\alpha_n]}.$$

Figure 1 shows the magnitudes $(\mathbf{q}_n, \sigma_n)$ and phases $(\mathbf{r}_n, \phi_n)$ of the spatial patterns and the time series of the first two modes $(n = 1, 2)$ obtained from the CEOF analysis. These modes account for the largest (75%) and second-largest (12%) amount of variance in the time series, respectively. The first mode [Fig. 1(A)] captures the annual cycle, displaying a very regular phase progression in time and a strong meridional asymmetry in phase spatial structure. The phase spatial structure along the equator indicates westward propagation; the node line located north of the equator in the central to eastern tropical Pacific is due to the influence of the Intertropical Convergence Zone (ITCZ) [20, 21]. The areas of smallest annual cycle magnitude in SST lie under the ITCZ and the South Pacific convergence zone (SPCZ), while the largest magnitudes are associated with areas of strong upwelling along the equator and the coast of South America.

The second mode [Fig. 1(B)] accounts for the largest amount of variance on interannual timescales, corresponding to periods of $2-7$ yrs, indicating the dominant mode of ENSO in the time series. The mode displays equatorially confined areas of largest magnitude in the central to eastern Pacific, with SST variation in this area largely in phase. El Niño events, for example the particularly strong 1997-1998 El Niño, are represented in the time series by high magnitude values and phase values near zero. La Niña events are also featured by high magnitude values but phase values near $\pm\pi$.

Using the phase time series from the first two modes, one can define a generalized phase difference

$$\delta\phi_{k,l}(t) = k\phi_1(t) - l\phi_2(t),$$

where $k, l \in \mathbb{Z}^+$. The two modes are said to be phase locked if the phase difference $\delta\phi_{k,l}$ is bounded, i.e. $|k\phi_1(t) - l\phi_2(t) - \epsilon| < \text{const.}$, where ϵ is the average phase shift between the two time series [22]. Figure 2(A) shows the probability distribution of the values $\delta\phi_{1,2}(t) \bmod 2\pi$, an indication of the strength of the 2:1 phase synchronization of ENSO to the annual cycle. As can be seen, observed ENSO variations are not truly phase-locked to the annual cycle, as the phase differences span the entire 2π range. However, there is evidence of partial phase synchronization, with certain phase differences about three times as likely as others. This partial synchronization indicates that at certain times the two modes are phase-locked while at other times the phases of the two modes "slip past" each other.

The phase synchronization of El Niño events is illustrated in Fig. 3, which shows the

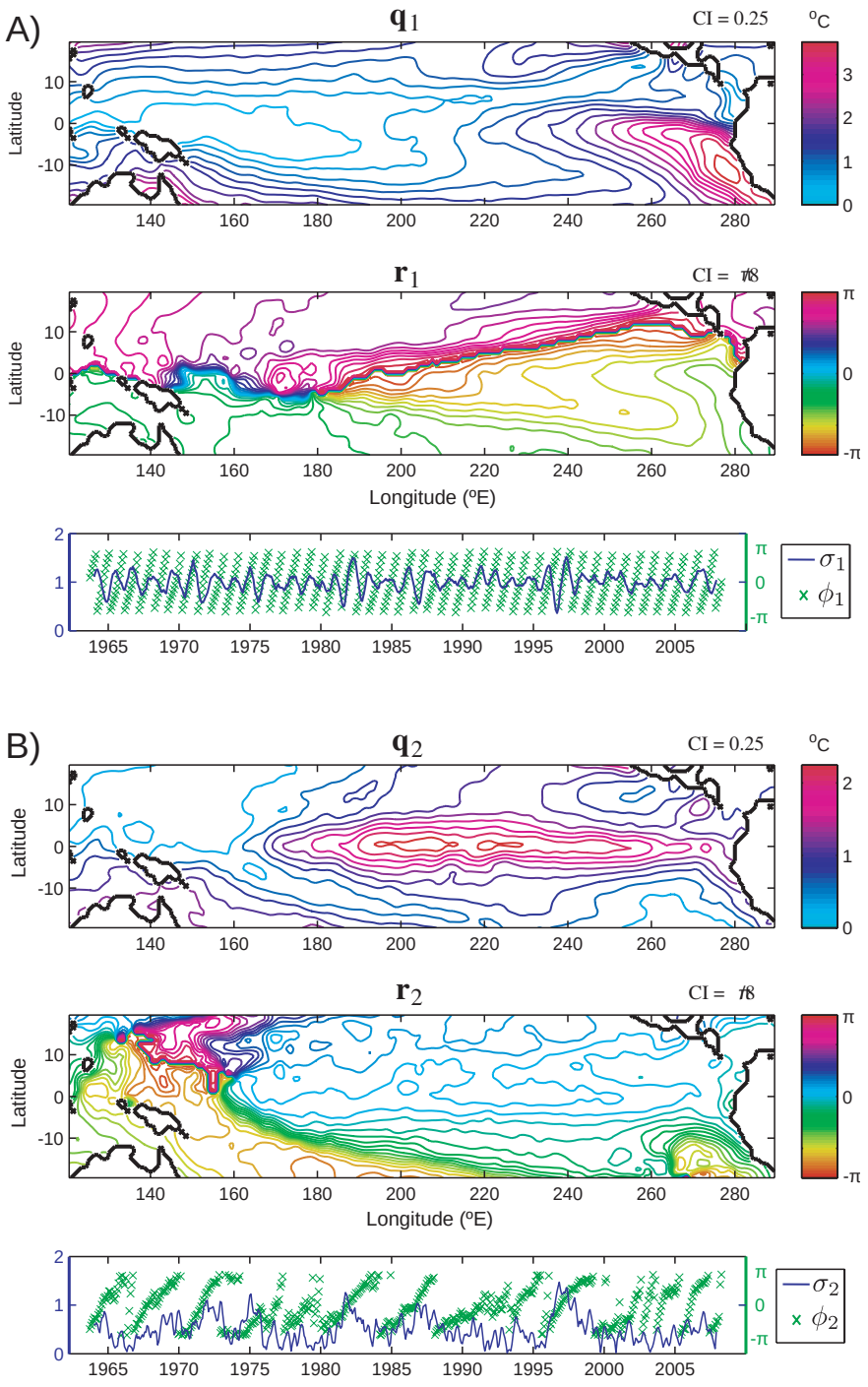

FIG. 1. The magnitudes $(\mathbf{q}_n, \sigma_n(t))$ and phases $(\mathbf{r}_n, \phi_n(t))$ associated with the first two modes obtained from a CEOF analysis of HadISST data. The contour plots show the spatial maps of $\mathbf{q}_n, \mathbf{r}_n$, with contour intervals indicated on the top right. The corresponding time series $\sigma_n(t)$ (blue line, left ordinate) and $\phi_n(t)$ (green x's, right ordinate) are shown below. The first mode (A) captures the seasonal cycle while the second mode (B) captures ENSO.

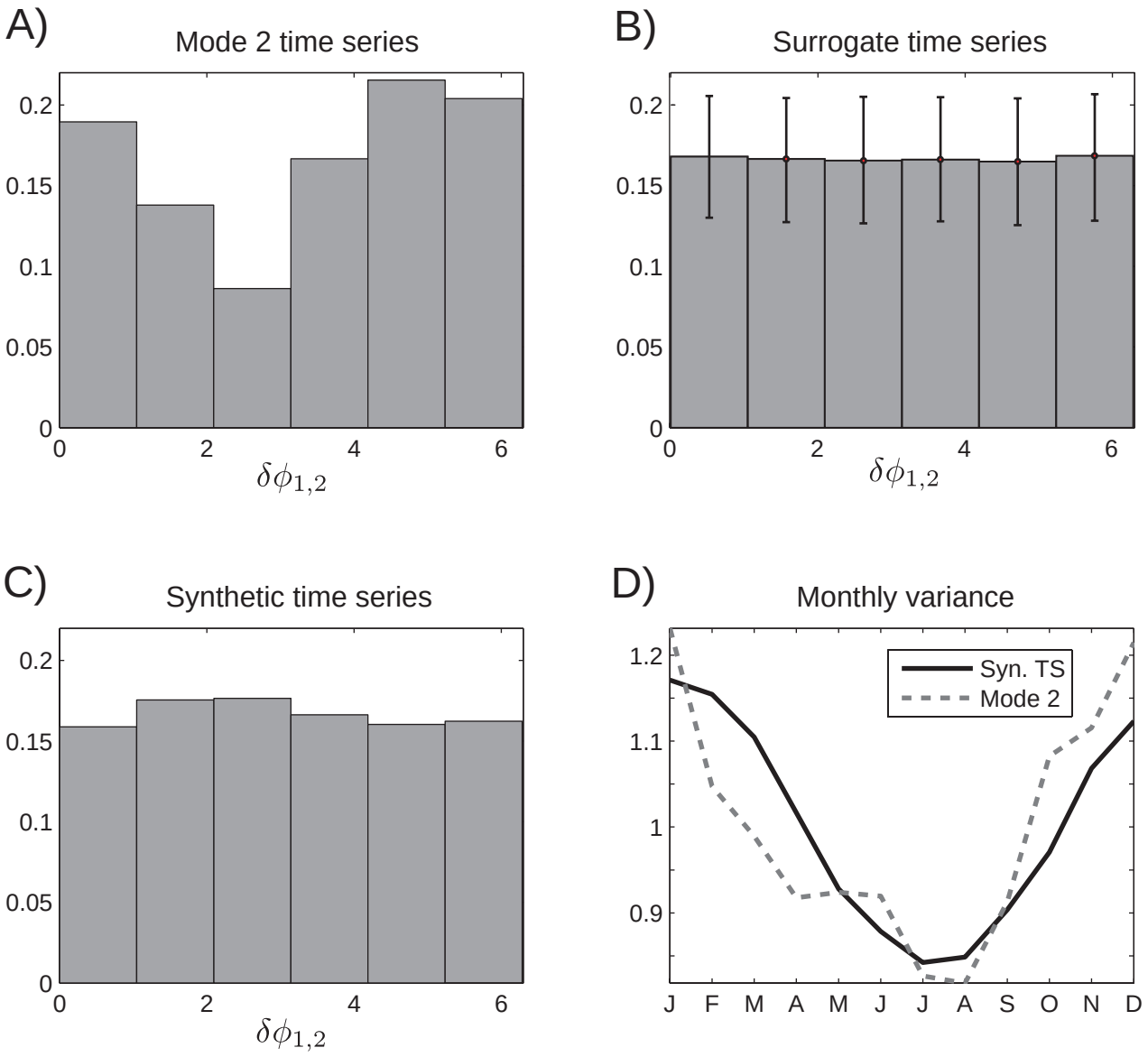

FIG. 2. Probabilty distributions of the phase difference $\delta\phi_{1,2}(t) \bmod 2\pi$, from the first two CEOF modes of HadISST observations (A), from surrogate time series (B), and from a synthetic time series based on a simple ENSO model (C). The errorbars indicate the 95% confidence intervals calculated from the surrogate time series (B). The monthly variance of the synthetic temperature series and the HadISST mode 2 time series are shown for comparison (D).

annual cycle phase portrait, with marker sizes proportional to the magnitude of the ENSO time series. Highlighted in red are points where the mode 2 temporal phase is near zero, corresponding to the warm El Niño phase, which tend to cluster in the bottom right quadrant of the annual cycle phase space, corresponding to boreal fall. The large magnitude El Niños

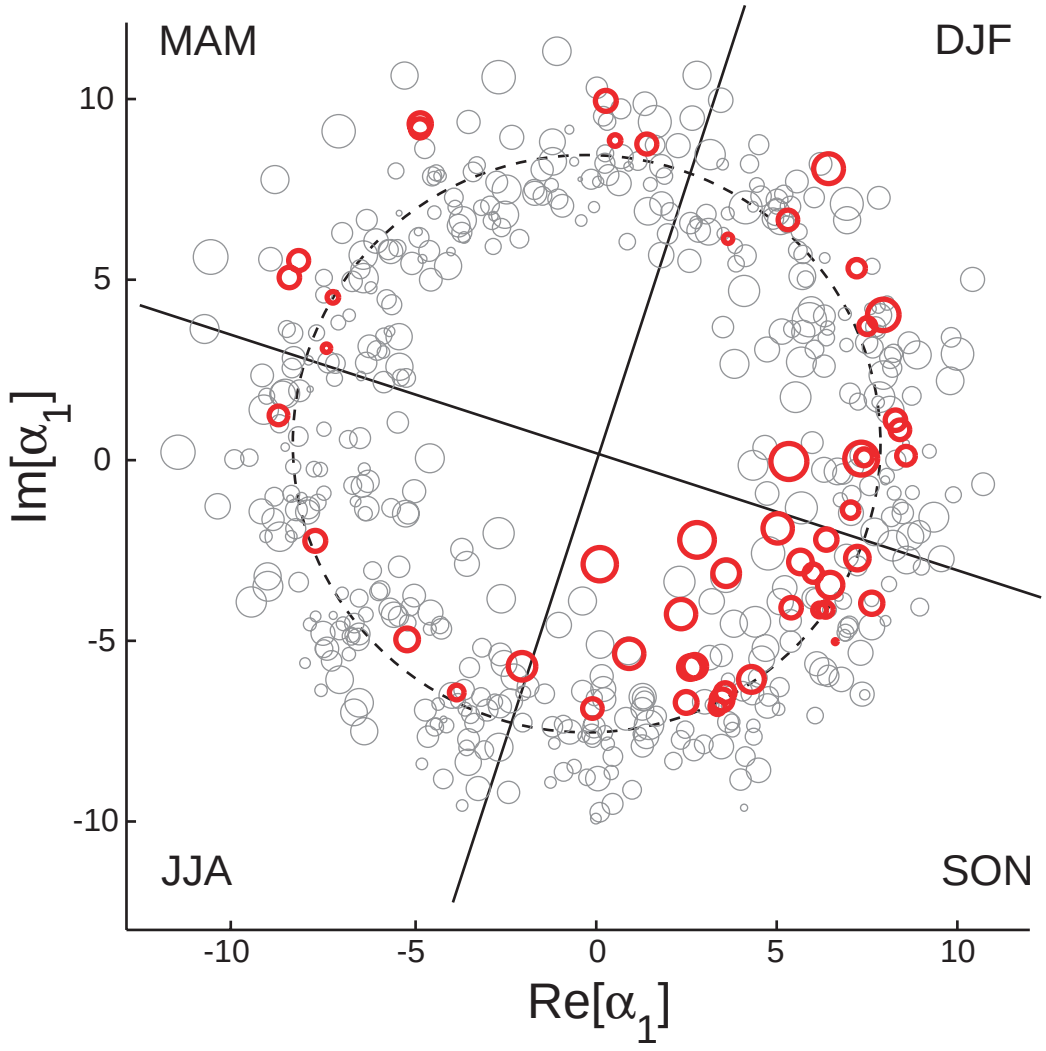

FIG. 3. Scatter plot of the mode 1 time series (α_1) with marker size proportional to the magnitude of the mode 2 time series (σ_2). Highlighted in red are points where the mode 2 temporal phase is near zero, corresponding to El Niño events ($-\frac{\pi}{9} \leq \phi_2 \leq \frac{\pi}{9}$). The figure is divided into seasonal quadrants, based on the monthly averages of the mode 1 temporal phase (ϕ_1). The composite seasonal cycle is shown as a dashed circle.

occur predominantly in this quadrant, and are associated with a weaker annual cycle [21]. The preferred $\delta\phi_{1,2}$ values tend to occur in boreal fall as well (not shown), which reflects the fact that the phase synchronization of the two modes does not persist through multiple annual cycles.

To test the significance of the range of observed phase differences, 1000 phase-randomized surrogate time series [23] were generated from the mode 2 time series $\alpha_2(t)$, using the

TISEAN software package [24], which employs an iterative algorithm that terminates when the variance spectrum and the probability distribution of the surrogates agree with that of the original time series [25]. The corresponding $\delta\phi_{1,2}(t)$ values were then calculated between $\alpha_1(t)$ and each surrogate time series. The distribution of the average of all $\delta\phi_{1,2}$ values and the 95% confidence intervals for each phase difference is shown in Fig. 2(B). Both the least-likely and most-likely observed phase differences [Fig. 2(A)] fall outside of the 95% confidence intervals [Fig. 2(B)], indicating that the observed $\delta\phi_{1,2}$ range is not an artefact of the length of the time series.

We then compared the results to output from a simple model of ENSO that has been shown to reproduce aspects the seasonal synchronization of ENSO events via amplitude modulation. The model, a version of the recharge oscillator [26] derived from the seasonally modulated Bjerknes index [27], estimates the first-order effect of the seasonal cycle on the stability of the coupled ocean-atmosphere system [16]. The equations take the form of a stochastically forced harmonic oscillator with periodically varying damping:

$$\frac{dT}{dt} = 2\gamma(t)\,T + \omega H + \zeta(t) \tag{1}$$

$$\frac{dH}{dt} = -\Omega T \tag{2}$$

where T represents eastern Pacific SST anomalies, H represents the mean thermocline depth anomaly across the Pacific basin, Ω provides the time scale for the slow basin-wide geostrophic adjustment of the mean thermocline depth to zonal wind stress anomalies, and $\zeta(t)$ is Gaussian white noise representing forcing by the atmosphere. For the demonstration here, the seasonal damping was prescribed as a simple sine wave with a damping rate varying between 0 and 1 yr^{-1}, and the parameters ω, Ω were set such that the mean frequency of the oscillator was 3.55 yr^{-1}. The output of the model was normalized to unit variance, so the strength of the white noise forcing is arbitrary. The model output T constitutes the synthetic ENSO time series, and the synthetic seasonal cycle is a simple sine wave with a period of one year.

Figure 2(D) shows the monthly variance of the HadISST mode 2 time series and that of the T time series from a 500 year integration of equations (1,2). The simple model displays a seasonal cycle of variance that is similar to the observed, with highest variance in boreal winter, indicating ENSO events tend to peak at this time. Often, this seasonal variance is interpreted as phase-locking; however, it is apparent that there is no phase interaction

between the synthetic seasonal cycle and the synthetic ENSO time series [Fig. 2(C)]. The synchronization of the idealized model events is due solely to amplitude modulation by the seasonal cycle, a linear mechanism that can reproduce the observed seasonal variance but cannot be distinguished from frequency modulation based on this criterion. The results presented here indicate that frequency modulation by the annual cycle plays at least some role in the observed seasonal synchronization of ENSO events, implying the importance of nonlinearities within the ocean-atmosphere system in this process.

In summary, we have provided, to our knowledge, the first observational evidence of partial *phase* synchronization of ENSO to the annual cycle. This evidence was based on the analysis of the first two modes generated by complex empirical orthogonal function analysis of sea surface temperature observations, which captured the seasonal cycle and ENSO as the first and second empirical modes. The 2:1 phase synchronization of ENSO to the annual cycle was examined by calculating the generalized phase difference between the two modes. The resulting phase differences were not bounded, but certain phase differences were found to be three times more likely than others, implying a partial phase synchronization. The results add a new item to the list of ENSO characteristics that are considered indicators of nonlinear ENSO dynamics, including its low-dimensionality [9], certain aspects of its predictability [10] and its skewness [28, 29]. Our diagnostic analysis can be applied as a tool to further assess the quality of numerical model simulations and predictions of ENSO.

This research was supported by the Office of Science (BER), U.S. Department of Energy, Grants No. DE-SC0005111 and DE- FG02-07ER64469, and by the Japan Agency for Marine-Earth Science and Technology (JAMSTEC), by NASA through grant No. NNX07AG53G, and by NOAA through grant No. NA09OAR4320075, which sponsor research at the International Pacific Research Center. This is IPRC publication XXXX and SOEST publication YYYY.

[1] J. Neelin, D. Battisti, A. Hirst, F. Jin, Y. Wakata, T. Yamagata, and S. Zebiak, Journal of Geophysical Research **103**, 14,261 (1998).

[2] M. J. McPhaden, S. E. Zebiak, and M. H. Glantz, "Science" **314**, 1740 (2006).

[3] E. Rasmusson and T. Carpenter, Monthly Weather Review **110**, 354 (1982).

[4] E. Tziperman, S. Zebiak, M. Cane, X. Yan, and B. Blumenthal, Journal of Climate **11**, 2191 (1998).

[5] A. Clarke and L. Shu, Geophysical Research Letters **27**, 771 (2000).

[6] E. Galanti and E. Tziperman, Journal of the Atmospheric Sciences **57**, 2936 (2000).

[7] J. Neelin, F. Jin, and H. Syu, Journal of Climate **13**, 2570 (2000).

[8] S. An and B. Wang, Journal of Climate **14** (2001).

[9] S. Bauer and M. Brown, Geophysical Research Letters **19**, 2055 (1992).

[10] J. Elsner and A. Tsonis, Geophysical Research Letters **20**, 213 (1993).

[11] F. Jin, J. Neelin, and M. Ghil, Science **264**, 70 (1994).

[12] E. Tziperman, S. Zebiak, and M. Cane, Journal of the Atmospheric Sciences **52** (1995).

[13] P. Chang, L. Ji, B. Wang, and T. Li, Journal of the Atmospheric Sciences **52** (1995).

[14] C. Thompson and D. Battisti, Journal of Climate **13**, 2818 (2000).

[15] R. Kallummal and B. Kirtman, Journal of the Atmospheric Sciences **65**, 3860 (2008).

[16] K. Stein, N. Schneider, A. Timmermann, and F. Jin, Journal of Climate **23**, 5629 (2010).

[17] N. A. Rayner, D. E. Parker, E. B. Horton, C. K. Folland, L. V. Alexander, D. P. Rowell, E. C. Kent, and A. Kaplan, Journal of Geophysical Research **108**, 4407 (2003).

[18] T. P. Barnett, "Monthly Weather Review" **111**, 756 (1983).

[19] R. W. Preisendorfer, *"Principal Component Analysis in Meteorology and Oceanography"*, Developments in Atmospheric Science, Vol. 17 (Elsevier Science Publisers B.V., 1988).

[20] J. Horel, Monthly Weather Review **110**, 1863 (1986).

[21] S. Xie, Journal of Climate **7**, 2008 (1994).

[22] A. Pikovksy, M. Rosenblum, and J. Kurths, International Journal of Bifurcation and Chaos **10**, 2291 (2000).

[23] S. T. and A. Schmitz, Physica D **142**, 346 (2000).

[24] R. Hegger, H. Kantz, and T. Schreiber, CHAOS **9**, 413 (1999).

[25] T. Schreiber, Physical Review Letters **77**, 635 (1996).

[26] F. Jin, Journal of the Atmospheric Sciences **54**, 811 (1997).

[27] F. Jin, S. Kim, and L. Bejarano, Geophysical Research Letters **33**, L23708 (2006).

[28] G. Burgers and D. Stephenson, Geophysical Research Letters **29**, 1027 (1999).

[29] S. An and F. Jin, Journal of Climate **17**, 2399 (2004).